


Article

Experimental Study of Pressure and Velocity Fluctuations Induced by Cavitation in a Small Venturi Channel

Linrong Zhang ¹, Guangjian Zhang ^{2,3,*}, Mingming Ge ⁴  and Olivier Coutier-Delgosha ^{3,4}

¹ Post-Doctoral Research Center of Control Science and Engineering, Jiangsu University, Zhenjiang 212013, China; zlrctc@126.com

² Research Center of Fluid Machinery Engineering and Technology, Jiangsu University, Zhenjiang 212013, China

³ CNRS, ONERA, Arts et Metiers Institute of Technology, Centrale Lille, University Lille, UMR 9014—LMFL—Laboratoire de Mécanique des Fluides de Lille—Kampé de Fériet, F-59000 Lille, France; ocoutier@vt.edu

⁴ Kevin T. Crofton Department of Aerospace and Ocean Engineering, Virginia Tech, Blacksburg, VA 24060, USA; mmge@vt.edu

* Correspondence: guangjian.zhang@ensam.eu

Received: 12 November 2020; Accepted: 5 December 2020; Published: 8 December 2020



Abstract: The purpose of this paper is to investigate experimentally the influence of the cavitation extent on the pressure and velocity fluctuations in a small convergent–divergent channel. The mean cavity length is determined from high-speed photography images. The mean pressure and the intensity of the pressure fluctuations are obtained from the transient pressure signals recorded by two pressure transducers at the inlet and outlet of the test section. The statistical turbulence quantities are derived from the instantaneous velocity fields measured by the laser-induced fluorescent particle image velocimetry (PIV-LIF) technique. The experimental results show that the decrease of the cavitation number (the increase in the extent of cavitation) leads to a rise in the turbulent fluctuations in the wake region due to the impact of vapour clouds collapsing, while the presence of a vapour phase is found to reduce the streamwise and cross-stream velocity fluctuations in the attached cavity. It might be attributed to two mechanisms: the presence of a vapour phase modifies the vortex-stretching process, and the cavitation compressibility damps out the turbulent fluctuations. Similar effects of cavitation are also observed in the pressure fluctuations.

Keywords: cavitation; venturi; cavity length; PIV

1. Introduction

Hydrodynamic cavitation is a complex phenomenon involving mass and heat transfer between liquid and vapour phases at nearly constant temperatures. It typically occurs in some widely used hydraulic machines, such as turbines, pumps and propellers, when the local pressure is reduced below the vapour pressure. In some cases, the pressure and velocity fluctuations induced by the intrinsic cavitation instability can cause severe problems, like performance decrease, material surface erosion, vibration and noise. In order to obtain a better physical understanding of this complex phenomenon, the simple geometry venturi channel or hydrofoil are often used for investigation instead of real hydraulic systems.

In the research of cavitation unsteadiness, the cavity length is an important parameter, since it is greatly associated with the cavitation regime. As reported by Leroux et al. [1], when the cavity length increased to be larger than half the hydrofoil chord length, the cavity was transformed from

quasi-steady to exhibiting a cyclic shedding of large-scale vapour clouds. Unfortunately, so far, there has not been a unified method to define the cavity length. The visual observation from high-speed images of cavitation is a practical way to determine the cavity length. Through averaging the grey levels of a large number of images, the mean boundary of the cavitation area could be obtained by designating a threshold value of the grey level to match the eyes' observations [2]. The maximum cavity length, often used as a characteristic dimension in the unstable cavitation with large-scale cloud shedding, is also determined based on the eyes' inspection [3]. However, this determination method is not precise and rather subjective. Dular et al. [4] found that the position of the maximum standard deviation of grey level is correlated well with the position of the strongest cavitation structure oscillation. Therefore, an objective method to define the mean cavity closure could be proposed based on the location of the maximum standard deviation. In recent years, this method has been accepted, and its applications could be found in References [5–8].

The unsteady behaviour of cavitation is evidently related to the pressure fluctuations that can be captured by means of wall pressure measurements. Leroux et al. [1] found that the peak of the pressure fluctuation intensity was located at the cavity closure through ten aligned pressure transducers flush-mounted along the suction side of a hydrofoil. Wang et al. [9] measured the periodic variation of the pressure accompanying the process of growth and breakup of the attached cavity, and they also detected the pressure rise caused by the propagating front of the re-entrant jet or the condensation shock. Ganesh et al. [3] revealed that the pressure rise associated with the propagation of condensation shocks was very weak (only a few kPa), while Wu et al. [10] captured a much higher pressure rise of collapse-induced shock waves, reaching hundreds of kPa.

The cavitation instability has an influence as well on the turbulent velocity fluctuations. In order to investigate turbulent–cavitation interactions experimentally, the most essential step is to measure the instantaneous velocity field in the cavitating flow. It is well-acknowledged that the particle image velocimetry (PIV) allows a global acquisition of instantaneous velocity vectors with a little perturbation in the flow field. However, the laser-induced fluorescent (LIF) particles need to be used instead of the conventional tracer particles when applying it to cavitating flows, such that the issue of a strong reflection from the liquid/vapour interface could be avoided. The PIV-LIF technique has been widely employed to obtain the mean and fluctuating velocity fields in cavitating flows, especially in the areas with low void fractions [11–15]. The experimental results in the cavity wake region put in evidence that the collapse of the vapour clouds is the primary mechanism of vorticity production and resultant increase of the turbulence level. The velocity field in the cavitation area with a high void fraction is hard to measure, since the presence of vapour bubbles between the side wall and the laser sheet can block the view of the camera on the illuminated plane. The work of Dular et al. [16,17] shows that if the position of the light sheet was close enough to the observation window (~ 5 mm), the detected particles would be sufficient to evaluate the velocity field inside the sheet cavity.

In the present paper, we investigated the cavitating flows developed in a 2D convergent–divergent channel at different flow rates and cavitation numbers through the techniques of high-speed photography, transient pressure measurement and PIV-LIF measurement. Based on the experimental results, the global parameters (pressure loss coefficient, outlet-to-inlet pressure ratio and mean cavity length) were correlated with the cavitation number, and the effects of cavitation on the pressure and velocity fluctuations were also analysed.

2. Experimental Setup and Methods

2.1. Hydraulic Test Rig

The venturi-type test section was connected to a closed-loop cavitation tunnel located in the Cavitation, Propulsion & Multiphase Flow Laboratory of Virginia Tech, Blacksburg, VA, USA, as shown in Figure 1. During the experiments, the flow circulation in the loop was driven by a centrifugal pump. The working fluid was tap water that was let to rest overnight prior to the measurements.

This action was for reducing the influence of the water–gas content on cavitation. The flow rate, measured by a turbine flow meter, was regulated by a frequency inverter varying the pump rotation speed. A secondary recirculation loop was added to attain small flow rates while avoiding the pump operating in off-design conditions. Different extents of the cavitation could be set properly by adjusting the pressure on the free surface of the tank with the aid of a vacuum pump or a pressuriser. A heater combined with a cooling system was employed, enabling the flow temperature to be maintained at a given value (20 °C in the present experiments) that was measured by a thermocouple located upstream of the test section.

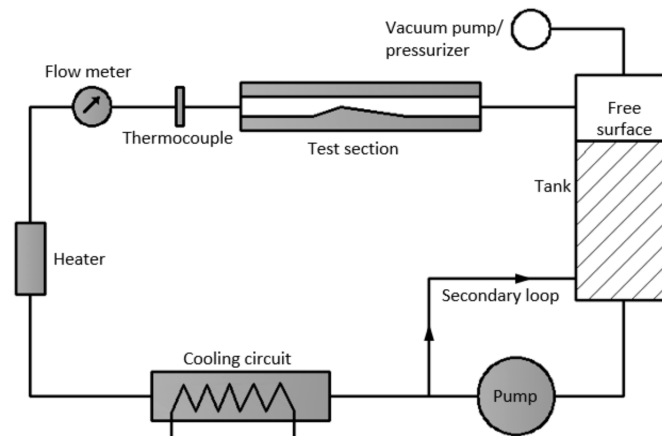


Figure 1. Schematic of the cavitation tunnel.

2.2. Multifunctional Venturi-Type Test Section

The side view of the test section is shown in Figure 2a. It was specially designed to be applicable in experiments of high-speed visualisation, particle image velocimetry (PIV) and in-line X-ray imaging. The rectangular area is zoomed and shown in Figure 2b. The base (1) and the lid (2) were made of non-transparent hard plastic through the 3D printing technique. Both of them constitute the main body of the test section. The bottom insert (3) acts as the convergent–divergent floor of the venturi section. The top insert (4) forms the ceiling of the venturi. The inserts (3) and (4) were both manufactured in glass rather than plexiglass, since the former has a better light transmittance and is less likely to be burned by an intense laser. The venturi profile is depicted by the black dashed lines. The heights at the inlet and the outlet are both 20 mm, and the height at the throat is 10 mm. The convergent and divergent angles of the venturi are 18° and 8°, respectively. The pressure sensor (5) was flush-mounted at the inlet, with another one (6) at the outlet.

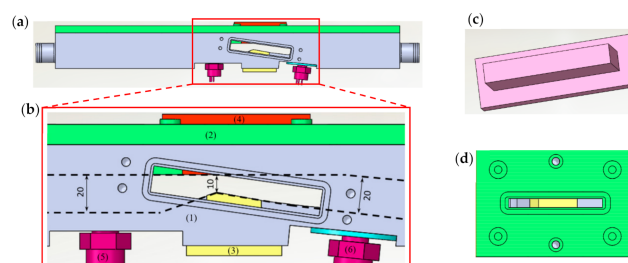


Figure 2. Test section—flow direction from left to right: (a) side view of the overall test section, (b) the enlarged convergent–divergent section, dimensions in mm, (c) side wall insert and (d) top view of the convergent–divergent section.

Two identical parts, as shown in Figure 2c, were inserted into the slots in the base (1) from the front and back, forming the observation window and, also, serving as the side walls of the venturi

channel. It should be noted that the two side inserts were made of plexiglass, as its refractive index is closer to water compared to normal glass. In the X-ray imaging experiments [18–20], the side insert was replaced by a hollow one with the thickness of only 0.5 mm. Figure 2d shows the top view after removing the top insert (4). The slot here is important for the PIV experiments, as it allows the calibration plate to be placed into the venturi channel. The channel width is only 5 mm in order to minimise the 3D effect of cavitation.

2.3. Pressure Measurements

The transient pressure at the inlet and the outlet was measured using two piezoresistive pressure sensors (Keller 10L series) calibrated in a range of 0–3 bar with a full-scale uncertainty of 0.25%. Signals from the pressure sensors were collected synchronously through a NI USB-6216 data acquisition card and exported to a computer by LabVIEW software. The sampling frequency was set to be 10 kHz, and the sample size was 10,000 (corresponding to a recording time of 1 s) for all flow conditions. Figure 3 shows an example of the pressure signals recorded by the inlet and outlet sensors. The averaged inlet pressure P_{in} was used to calculate the cavitation number σ :

$$\sigma = \frac{P_{in} - P_{vap}}{0.5\rho u_{in}^2}, \quad (1)$$

where P_{vap} is the vapour pressure at the flow temperature, u_{in} is the bulk velocity at the inlet computed according to the volumetric flow rate measured by the flow meter and ρ is the liquid density. The uncertainty in computing the cavitation number caused by the accuracies of the pressure and velocity measurements is estimated to be 3.5%. It can be seen qualitatively from Figure 3 that the pressure fluctuation intensity at the outlet is much more intense than that at the inlet due to the occurrence of cavitation.

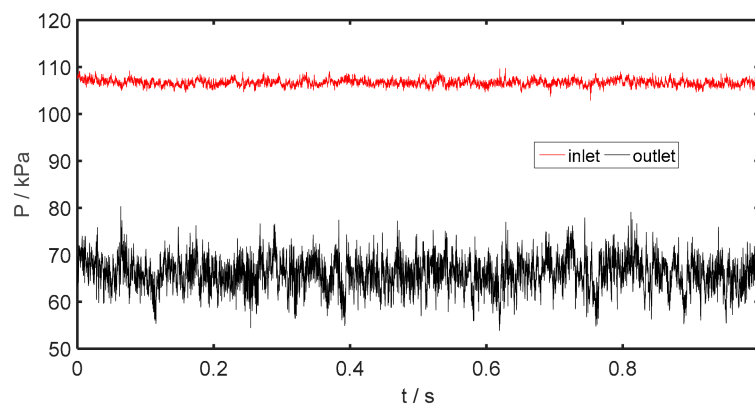


Figure 3. An example of the pressure signals recorded by the inlet and outlet sensors ($\sigma = 2.08$, $u_{in} = 10$ m/s).

2.4. High-Speed Visualisation

The cavitation structures produced in the throat region of the venturi were captured from the side using a high-speed Photron Fastcam SA 1.1 camera equipped with a Tokina 100-mm lens. A high-power continuous light source was fixed above the test section. It illuminated the convergent–divergent section where the cavitation develops through the glass insert (4) shown in Figure 2b. The camera frame rate was set to 8000 frames per second (fps), with a short exposure time of 10 μ s to freeze the fast-moving cavitation structures. The field of view was 1024×512 pixels, with each pixel corresponding to 30 μ m. Figure 4 shows a typical snapshot of cavitation in the area of interest selected from a high-speed photograph sequence. The image was recorded in grey scale of an 8-bit resolution (0 for black pixel and 255 for white pixel). The two-phase cavitation structures reflect light more strongly, resulting in

higher grey levels in the recorded image, while the dark area indicates the presence of the liquid phase. A high-speed image sequence would be used to estimate the mean cavity length.

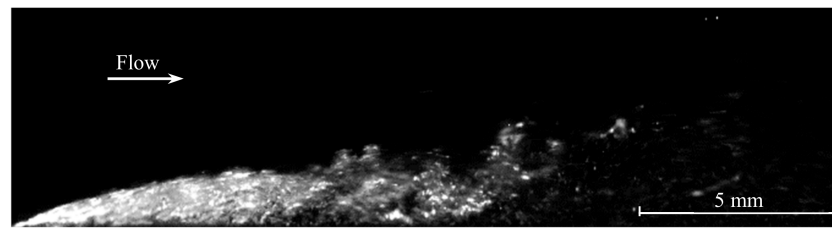


Figure 4. A typical snapshot showing the instantaneous cavity shape ($\sigma = 2.38$, $u_{in} = 9.33$ m/s).

2.5. PIV-LIF Measurements

The velocity fields in the cavitating flows were measured using a LaVision PIV system. The light source in the present experiments was a double-pulsed Nd:YAG laser with a pulse duration of 10 ns. The laser beam was expanded by a cylindrical lens into a light sheet with thickness of about 1 mm for illuminating the centre plane of the venturi channel. The energy density in the laser sheet could be adjusted to sufficiently high, as it goes through the replaceable glass inserts that are less likely to be damaged.

Before starting the circulating pump, a calibration plate shown in Figure 5 was placed in the centre plane of the venturi channel filled with water. The purpose of this step was to define the scale factor (mm/pixel) and eliminate the perspective and refraction errors. The coordinate system used was also defined during the calibration process. The x-axis is along the venturi divergent floor, and the origin is located at the venturi throat edge.

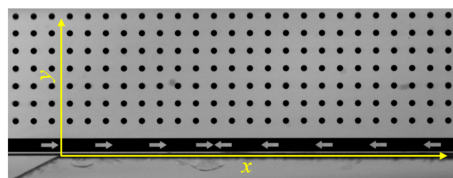


Figure 5. Calibration plate with a regular distribution of marks. The dot diameter is 0.33 mm, and the distance between dots is 1 mm. The coordinate system used is also defined.

The fluorescent particles (Rhodamin B, diameter of around 20 μm) were added to the cavitating flow as the liquid phase tracers. They absorb the laser light with the wavelength of 532 nm and emit light at 584 nm. An optical notch filter at 532 nm from EO Edmund was mounted in front of the camera lens. In this way, the reflected laser light (remaining at the wavelength of 532 nm) from the two-phase structures is blocked by the notch filter, and only the light emitted from the fluorescent particles is recorded. For each operating condition, 2000 pairs of particle images were acquired by a high-speed CCD camera at a frequency of 2000 Hz. The spatial resolution of the raw images was 1024×512 pixels. The time delay between the two images of the same pair varied from 8 to 12 μs , depending on the flow velocity for achieving a particle shift of about 5 pixels.

A raw particle image in the area of interest is presented in Figure 6a. As can be seen, the cavitation structure is still visible in the image, as it reflects light emitted from the fluorescent particles. Its contaminating effect on the particle image could be reduced through performing a high-pass Gaussian filter, and the processed image is shown in Figure 6b. On the other side, the number of detected particles is indeed influenced by the presence of the vapour/liquid mixture. It is attributed to two reasons: (a) vapour structures between the laser sheet and the side wall block the fluorescent particles in the illuminated plane; this problem is not the primary cause for less-detected particles in the present experiments, since the measurement plane is close enough to the front observation

window (only 2 mm), and (b) the cavity of higher vapour contents can carry fewer particles; as a consequence, few particles are distinguished in the upstream attached cavity, while the particle density in the detached vapour clouds is less decreased.

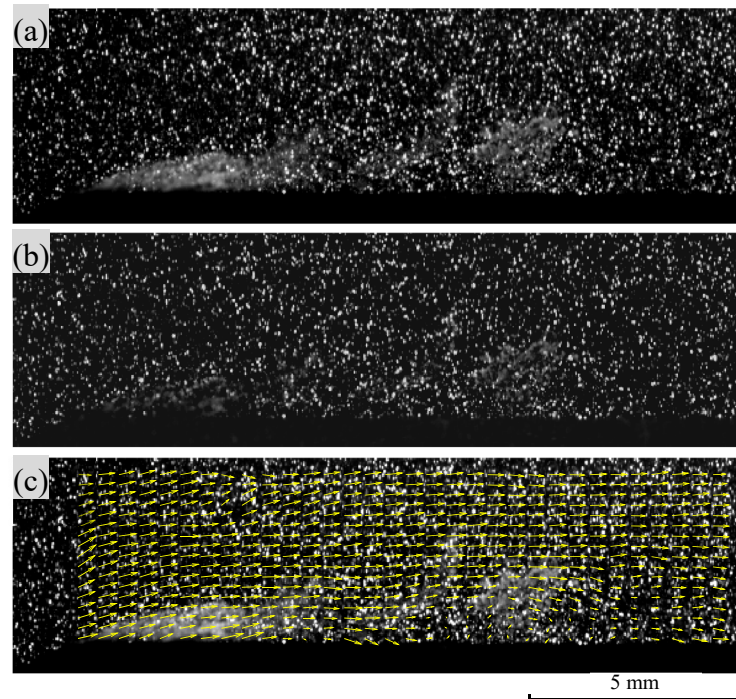


Figure 6. An example of evaluating an instantaneous velocity field in the cavitating flow ($\sigma = 2.49$, $u_{in} = 0.85$ m/s) (a) raw PIV image, (b) processed image with a high-pass Gaussian filter and (c) instantaneous velocity vector field (every second vector is displayed in the horizontal direction for clarity).

The instantaneous velocity fields were evaluated using the iterative cross-correlation algorithm in the software Davis 8.1 from LaVision. The interrogation window for the first pass was 64×64 pixels, followed by 2 passes with interrogation windows of 16×16 pixels, and an overlap of 50% was used. The correlation peak was determined with a subpixel accuracy by using the three-point Gaussian fitting scheme in two directions. The particle density was taken into account in the final pass, where the vectors in the interrogation windows with less than 4 particles were rejected and replaced by a bilinear interpolation from their valid neighbouring vectors. This implied that the calculated velocities in the attached cavity had a higher uncertainty, as the particle concentration there was not sufficient. Figure 6c shows a velocity vector field evaluated using the above algorithm.

3. Results and Discussion

3.1. Pressure Loss versus Cavitation Number

The extent of cavitation is described primarily by the cavitation number that can be varied through adjusting the inflow velocity and inlet pressure in the experiments. The absolute pressure loss $P_l = P_{in} - P_{out}$, defined as the difference between the average inlet and outlet pressures, is evidently related to the degree of cavitation. As shown in Figure 7a, decreasing the cavitation number results in an increase of the cavitation area, and consequently, the absolute pressure loss is increased over the convergent-divergent channel due to the flow blockage effect. In addition, the absolute pressure loss is positively correlated with the inflow velocity u_{in} . Figure 7b presents the relationship between the cavitation number and the pressure loss $P_{l,c} = (P_{in} - P_{out}) / 0.5\rho u_{in}^2$ normalised by the inlet dynamic pressure. It can be seen that all experimental points collapse well around one curve, suggesting that

the normalised pressure loss is only a function of the cavitation number, independent of the inflow velocity. This result is consistent with the measurements of Jahangir et al. [21] in an axisymmetric converging–diverging nozzle. Another parameter of the pressure ratio $P_r = P_{out}/P_{in}$ is also plotted as a function of the cavitation number shown in Figure 7c, and it is observed to be also independent of the inflow velocity.

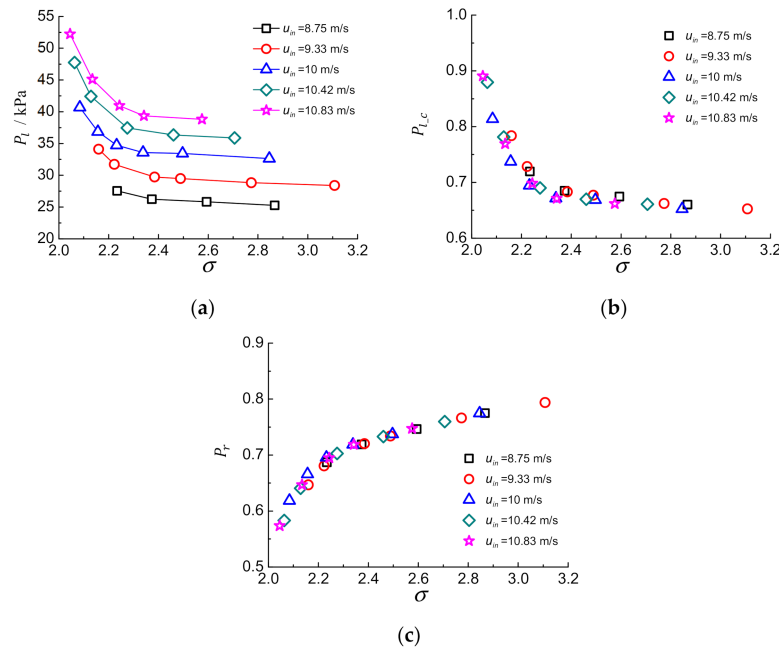


Figure 7. The pressure loss as a function of the cavitation number σ : (a) absolute pressure loss, P_l ; (b) pressure loss coefficient P_{l_c} and (c) outlet-to-inlet pressure ratio P_r .

3.2. Cavity Length versus Cavitation Number

In the present work, the mean cavity length was evaluated based on the distribution of the standard deviation of grey level of a sequence of high-speed images. The location of the maximum standard deviation was used to define the position of the mean cavity closure, and consequently, the mean cavity length was determined as the distance from the venturi throat to the location of the maximum standard deviation. This criterion was applied to all the measured flow conditions, regardless of cavitation regime of small oscillation or large-scale shedding. For each operating point, 2000 high-speed images were recorded to estimate the mean cavity length. Figure 8 shows an example of the influence of the number of the images used to calculate the mean value and the standard deviation of the grey levels. The convergence test was performed exactly at the position of the maximum standard deviation determined from 2000 images. As can be seen, when the image number is greater than 1500, the mean value and the standard deviation of the grey levels tend to stabilise in a small range of ± 0.5 . Therefore, 2000 images would be sufficient to evaluate the mean cavity length.

The nondimensional mean cavity length $L_{cav}^* = L_{cav}/H_{th}$ is illustrated in Figure 9 as a function of the cavitation number for different inflow velocities. Here, L_{cav} is the mean cavity length derived from the above procedures, and H_{th} is the height at the venturi throat. It can be found that, similar to the pressure loss coefficient, all the measurement points of the mean cavity length collapse on one curve again, indicating that the mean cavity length is only dependent on the cavitation number, irrespective of the inflow velocity. With the reduction of the cavitation number, the mean cavity length is, as expected, increased. However, a critical cavitation number at around 2.4 could be identified—on the two sides of which, the ratio of the cavity length variation is quite different. For the flow conditions with the cavitation number greater than the critical value, the attached cavity appears to be relatively steady,

whereas, when the cavitation number is lower than the critical value, the slight change could lead to a strong influence on the extent of the cavitation. This phenomenon was also reported by Long et al. [7].

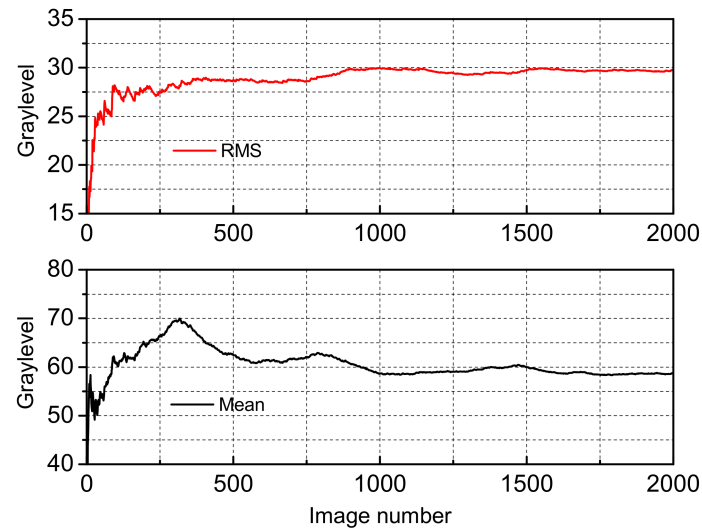


Figure 8. Convergence test of the mean value and the standard deviation of the grey levels ($\sigma = 2.23$, $u_{in} = 10$ m/s).

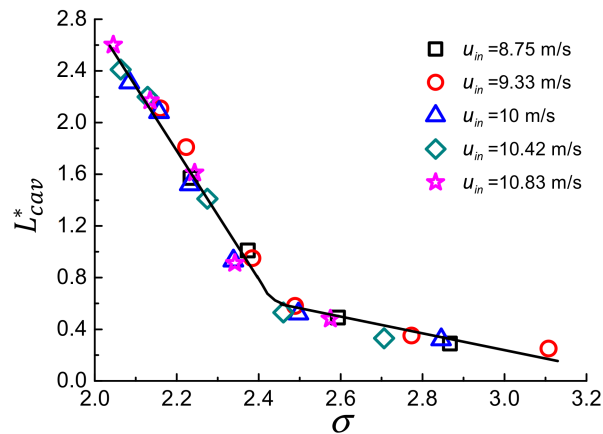


Figure 9. The nondimensional mean cavity length as a function of the cavitation number. The curve fits through the measurement points.

3.3. Velocity and Pressure Fluctuations

Based on 2000 instantaneous velocity fields evaluated from the PIV measurements, we could obtain the statistical turbulence properties: the streamwise velocity fluctuation u'^* , the cross-stream velocity fluctuation v'^* and the primary Reynolds shear stress $u'v'^*$. Their definitions are given as follows:

$$u'^* = \sqrt{\overline{u'u'}}/u_{ref} \quad (2)$$

$$v'^* = \sqrt{\overline{v'v'}}/u_{ref} \quad (3)$$

$$u'v'^* = \sqrt{\overline{u'v'}}/u_{ref} \quad (4)$$

where u_{ref} is the bulk velocity at the venturi throat. In order to investigate the effects of the cavitation on turbulent velocity fluctuations, the mean cavity length should be of slight difference for the measured

cavitation numbers to ensure similar dynamics. In the present work, four relatively high cavitation numbers ($\sigma = 2.63, 2.55, 2.49$ and 2.42) were selected according to the relationship between the cavity length and cavitation number in Figure 9. These four flow conditions yield a similar cavitation regime that is characterised by a relatively stable cavity, with small vapour shedding in the closure region. The vapour volume fraction in the attached cavities is relatively low, such that more tracer particles can be carried and detected for the cross-correlation operation. Since the mean cavity length is around 6 mm for the studied cases, two vertical stations were identified: $x = 3$ mm within the attached cavity and $x = 12$ mm in the cavity wake where the detached vapour clouds collapse.

The profiles of u'^* , v'^* and $u'v'^*$ for the different cavitation numbers at $x = 3$ mm and $x = 12$ mm are presented in Figure 10a,b, respectively. It is clear that the decrease of the cavitation number leads to a rise in the turbulent fluctuations for all the three components in the wake region due to the impact of the cavitation collapse. This is in a good agreement with the experimental results reported by Gopalan and Katz [11] and Laberteaux and Ceccio [12]. On the other hand, the presence of a vapour phase is observed to reduce the streamwise and cross-stream velocity fluctuations in the attached cavity. This finding is consistent with the measurement results by fast X-ray imaging [19,22] and the simulation results in a similar venturi nozzle [23]. Two mechanisms might be responsible for the suppression effect of cavitation on turbulence: (1) As suggested by Belahadji et al. [24], the presence of a vapour phase modifies the vortex-stretching process; for a noncavitating vortex, its diameter would reduce as it is stretched; in order to satisfy the conservation of angular momentum, the rotation rate increases, and consequently, the pressure at the vortex core decreases; however, the core of a cavitating vortex can remain a constant pressure, which limits the vorticity production due to vortex stretching; the numerical results by large eddy simulation [23,25] also verified that the cavitation decreases the vortex-stretching term. (2) The sound speed in the vapour/liquid mixtures could be reduced to a few meters per second [26,27], which makes the cavitation structures highly compressible; as presented by Barre et al. [28], the flow compressibility has a tendency to damp out the turbulent fluctuations. The effect of the presence of vapour on Reynolds shear stress $u'v'^*$ is not clear, since the correlation between the streamwise and cross-stream velocity fluctuations seems not to be dependent on the variation of the cavitation number.

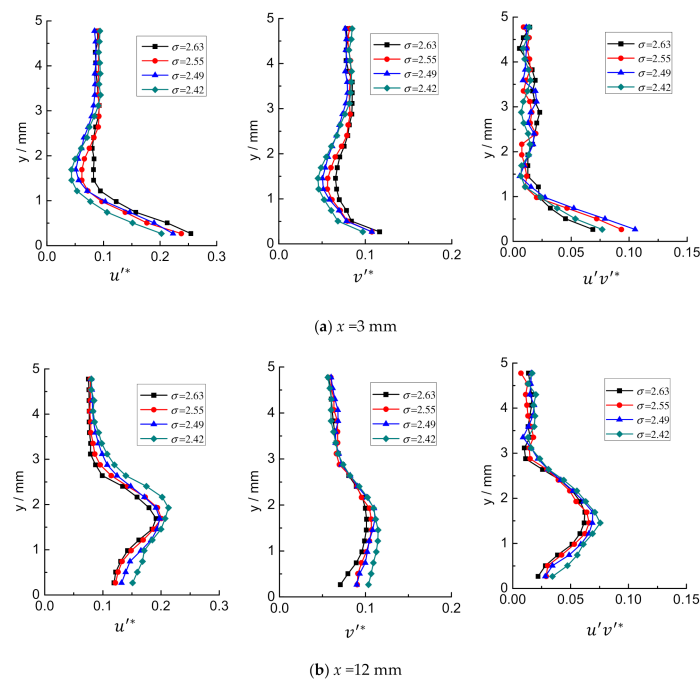


Figure 10. (a) Profiles of u'^* , v'^* and $u'v'^*$ for different cavitation numbers at $x = 3$ mm. (b) Profiles of u'^* , v'^* and $u'v'^*$ for different cavitation numbers at $x = 12$ mm.

The average pressure fluctuation intensity was derived from the standard deviation of the pressure signal recorded by the sensors. Figure 11a,b illustrates the intensity of the pressure fluctuations (P'_{in} and P'_{out}) normalised by the inlet dynamic pressure at the inlet and outlet, respectively. As expected, with decreasing the cavitation number, the collapse of vapour bubbles leads to an increase in pressure fluctuations at the venturi outlet. This trend is more pronounced in the flow conditions with lower cavitation numbers. On the contrary, the pressure fluctuations at the inlet present a global trend of decrease with the extent of cavitation, suggesting that the pressure fluctuations upstream of the cavity are suppressed due to the presence of two-phase cavitation structures. This is consistent with the effect on the velocity fluctuations. However, the different trend is identified at higher cavitation numbers: an increase in the extent of the cavitation results in a rise of pressure fluctuations at the inlet. One possible interpretation is that the small amount of vapour presence at higher cavitation numbers does not yield a significant dampening on the pressure fluctuations, while the cavitation collapse plays the major role.

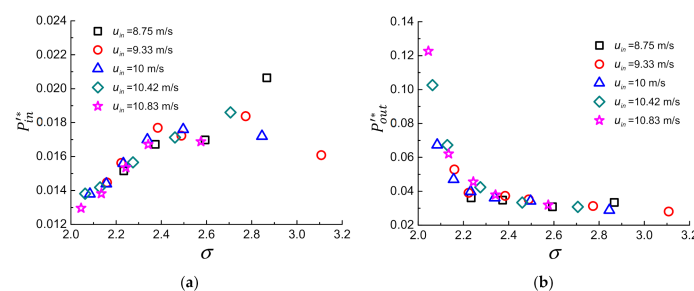


Figure 11. Nondimensional pressure fluctuation intensity with respect to the cavitation number: (a) P'_{in} at the venturi inlet and (b) P'_{out} at the venturi outlet.

4. Conclusions

An experimental investigation of cavitating flows in a venturi-type test section was performed with the emphasis on the pressure and velocity fluctuations induced by cavitation. The test section featured with replaceable inserts was specially designed to make it applicable in the experiments of high-speed visualisation, particle image velocimetry (PIV) and in-line X-ray imaging. The two piezoresistive pressure transducers were flush-mounted at the venturi inlet and outlet to record simultaneously the transient pressure signals, based on which, the mean pressure and the intensity of the pressure fluctuations could be obtained. The high-speed visualisation was carried out to capture a sequence of images of the cavitation structures from the side view. The mean cavity length was determined in an objective way; the location of the maximum standard deviation of grey levels of high-speed images was considered as the position of the cavity closure, which avoids choosing the threshold value empirically. The instantaneous velocity fields in the cavitating flows were measured through the PIV-LIF technique. The combined use of fluorescent particles with an optical notch filter eliminated the strong laser reflection from the opaque two-phase structures. In order to detect more tracer particles in the region occupied by cavitation bubbles, the venturi channel width was reduced down to only 5 mm, such that the blocking effect of the vapour bubbles (existing between the laser sheet and the observation window) on the illuminated particles could be alleviated. Moreover, the PIV measurements were conducted at flow conditions with higher cavitation numbers where the attached sheet cavity was able to carry more tracer particles. Based on the experimental results, the global parameters of the pressure loss coefficient, pressure ratio and mean cavity length were plotted with respect to the cavitation number. It was found that these parameters were only a function of the cavitation number, independent of the inflow velocity. In order to investigate the effects of cavitation on turbulent velocity fluctuations, two vertical stations were selected: one within the attached cavity and another in the cavity wake. It was observed that the collapse of vapour clouds resulted in a rise of turbulence level, while the presence of the attached cavity suppressed the velocity fluctuations.

The effects of cavitation on the intensity of the pressure fluctuations were found to be consistent with that on the velocity fluctuations.

Author Contributions: Writing—original draft preparation, G.Z.; writing—review and editing, L.Z.; funding acquisition, L.Z.; validation, M.G. and supervision, O.C.-D. All authors have read and agreed to the published version of the manuscript.

Funding: This research was funded by the China Postdoctoral Science Foundation (Grant No. 2020M671377).

Conflicts of Interest: The authors declare no conflict of interest.

References

1. Leroux, J.B.; Jacques, A.; Billard, J.Y. An experimental study of unsteady partial cavitation. *J. Fluids Eng.* **2004**, *126*, 94–101. [\[CrossRef\]](#)
2. Coutier-Delgosha, O.; Devillers, J.F.; Pichon, T.; Vabre, A.; Woo, R.; Legoupil, S. Internal structure and dynamics of sheet cavitation. *Phys. Fluids* **2006**, *18*, 017103. [\[CrossRef\]](#)
3. Ganesh, H.; Mäkiharju, S.A.; Ceccio, S.L. Bubbly shock propagation as a mechanism for sheet-to-cloud transition of partial cavities. *J. Fluid Mech.* **2016**, *802*, 37–78. [\[CrossRef\]](#)
4. Dular, M.; Bachert, B.; Stoffel, B.; Širok, B. Relationship between cavitation structures and cavitation damage. *Wear* **2004**, *257*, 1176–1184. [\[CrossRef\]](#)
5. Danlos, A.; Ravelet, F.; Coutier-Delgosha, O.; Bakir, F. Cavitation regime detection through Proper Orthogonal Decomposition: Dynamics analysis of the sheet cavity on a grooved convergent–divergent nozzle. *Int. J. Heat Fluid Flow* **2014**, *47*, 9–20. [\[CrossRef\]](#)
6. Prothin, S.; Billard, J.Y.; Djeridi, H. Image processing using proper orthogonal and dynamic mode decompositions for the study of cavitation developing on a NACA0015 foil. *Exp. Fluids* **2016**, *57*, 157. [\[CrossRef\]](#)
7. Long, X.; Zhang, J.; Wang, J.; Xu, M.; Ji, B. Experimental investigation of the global cavitation dynamic behavior in a venturi tube with special emphasis on the cavity length variation. *Int. J. Multiph. Flow* **2017**, *89*, 290–298. [\[CrossRef\]](#)
8. Zhang, H.; Zuo, Z.; Mørch, K.A.; Liu, S. Thermodynamic effects on Venturi cavitation characteristics. *Phys. Fluids* **2019**, *31*, 097107.
9. Wang, C.; Huang, B.; Wang, G.; Zhang, M.; Ding, N. Unsteady pressure fluctuation characteristics in the process of breakup and shedding of sheet/cloud cavitation. *Int. J. Heat Mass Transf.* **2017**, *114*, 769–785. [\[CrossRef\]](#)
10. Wu, X.; Maheux, E.; Chahine, G.L. An experimental study of sheet to cloud cavitation. *Exp. Therm. Fluid Sci.* **2017**, *83*, 129–140. [\[CrossRef\]](#)
11. Gopalan, S.; Katz, J. Flow structure and modeling issues in the closure region of attached cavitation. *Phys. Fluids* **2000**, *12*, 895–911. [\[CrossRef\]](#)
12. Laberteaux, K.R.; Ceccio, S.L. Partial cavity flows. Part 1. Cavities forming on models without spanwise variation. *J. Fluid Mech.* **2001**, *431*, 1–41. [\[CrossRef\]](#)
13. Iyer, C.O.; Ceccio, S.L. The influence of developed cavitation on the flow of a turbulent shear layer. *Phys. Fluids* **2002**, *14*, 3414–3431. [\[CrossRef\]](#)
14. Foeth, E.J.; Van Doorne, C.W.H.; Van Terwisga, T.; Wieneke, B. Time resolved PIV and flow visualization of 3D sheet cavitation. *Exp. Fluids* **2006**, *40*, 503–513. [\[CrossRef\]](#)
15. Kravtsova, A.Y.; Markovich, D.M.; Pervunin, K.S.; Timoshevskiy, M.V.; Hanjalic, K. High-speed visualization and PIV measurements of cavitating flows around a semi-circular leading-edge flat plate and NACA0015 hydrofoil. *Int. J. Multiph. Flow* **2014**, *60*, 119–134. [\[CrossRef\]](#)
16. Dular, M.; Bachert, R.; Stoffel, B.; Širok, B. Experimental evaluation of numerical simulation of cavitating flow around hydrofoil. *Eur. J. Mech. B Fluid* **2005**, *24*, 522–538. [\[CrossRef\]](#)
17. Dular, M.; Bachert, R.; Schaad, C.; Stoffel, B. Investigation of a re-entrant jet reflection at an inclined cavity closure line. *Eur. J. Mech. B Fluid* **2007**, *26*, 688–705. [\[CrossRef\]](#)
18. Khelifa, I.; Vabre, A.; Hočevár, M.; Fezzaa, K.; Fuzier, S.; Roussette, O.; Coutier-Delgosha, O. Fast X-ray imaging of cavitating flows. *Exp. Fluids* **2017**, *58*, 157. [\[CrossRef\]](#)

19. Zhang, G.; Khelifa, I.; Coutier-Delgosha, O. Experimental investigation of turbulent cavitating flows in a small venturi nozzle. In Proceedings of the ASME-JSME-KSME 2019 Joint Fluids Engineering Conference, San Francisco, CA, USA, 28 July–1 August 2019.
20. Zhang, G.; Khelifa, I.; Fezzaa, K.; Ge, M.; Coutier-Delgosha, O. Experimental investigation of internal two-phase flow structures and dynamics of quasi-stable sheet cavitation by fast synchrotron X-ray imaging. *Phys. Fluids* **2020**, *32*, 113310. [[CrossRef](#)]
21. Jahangir, S.; Hogendoorn, W.; Poelma, C. Dynamics of partial cavitation in an axisymmetric converging-diverging nozzle. *Int. J. Multiph. Flow* **2018**, *106*, 34–45. [[CrossRef](#)]
22. Karathanassis, I.K.; Koukouvinis, P.; Kontolatis, E.; Lee, Z.; Gavaises, M. High-speed visualization of vortical cavitation using synchrotron radiation. *J. Fluid Mech.* **2018**, *838*, 148–164. [[CrossRef](#)]
23. Dittakavi, N.; Chunekar, A.; Frankel, S. Large Eddy Simulation of Turbulent-Cavitation Interactions in a Venturi Nozzle. *J. Fluids Eng.* **2010**, *132*, 121301. [[CrossRef](#)]
24. Belahadji, B.; Franc, J.P.; Michel, J.M. Cavitation in the rotational structures of a turbulent wake. *J. Fluid Mech.* **1995**, *287*, 383–403. [[CrossRef](#)]
25. Xing, T.; Li, Z.; Frankel, S.H. Numerical simulation of vortex cavitation in a three-dimensional submerged transitional jet. *J. Fluids Eng.* **2005**, *127*, 714–725. [[CrossRef](#)]
26. Shamsborhan, H.; Coutier-Delgosha, O.; Caignaert, G.; Nour, F.A. Experimental determination of the speed of sound in cavitating flows. *Exp. Fluids* **2010**, *49*, 1359–1373. [[CrossRef](#)]
27. Brennen, C.E. *Cavitation and Bubble Dynamics*; Cambridge University Press: Cambridge, UK, 2013.
28. Barre, S.; Quine, C.; Dussauge, J.P. Compressibility effects on the structure of supersonic mixing layers: Experimental results. *J. Fluid Mech.* **1994**, *259*, 47–78. [[CrossRef](#)]

Publisher’s Note: MDPI stays neutral with regard to jurisdictional claims in published maps and institutional affiliations.



© 2020 by the authors. Licensee MDPI, Basel, Switzerland. This article is an open access article distributed under the terms and conditions of the Creative Commons Attribution (CC BY) license (<http://creativecommons.org/licenses/by/4.0/>).